Available online at www.sciencedirect.com
SCIENCE DIRECT®
ELSEVIER
Applied Surface Science 219 (2003) 211–227
applied surface science
www.elsevier.com/locate/apsusc

Computational analysis of the interfacial bonding between feed-powder particles and the substrate in the cold-gas dynamic-spray process

M. Grujicic[a,*], J.R. Saylor[a], D.E. Beasley[a], W.S. DeRosset[b], D. Helfritch[b]

[a]*Department of Mechanical Engineering, 241 Engineering Innovation Building, Clemson University, Clemson, SC 29634-0921, USA*
[b]*Army Research Laboratory-Processing and Properties Branch, Proving Ground, Aberdeen, MD 21005-5069, USA*

Received 29 March 2003; received in revised form 27 April 2003; accepted 27 April 2003

Abstract

The cold-gas dynamic-spray process is analyzed by numerical modeling of the impact between a single spherical feed-powder particle and a semi-infinite substrate. The numerical modeling approach is applied to the copper–aluminum system to help explain experimentally observed higher deposition efficiencies of the copper deposition on aluminum than the ones associated with the aluminum deposition on copper. To properly account for the high strain, high strain-rate deformation behavior of the two materials, the appropriate linear-elastic rate-dependent, temperature-dependent, strain-hardening materials constitutive models are used. The results obtained indicate that the two main factors contributing to the observed higher deposition efficiency in the case of copper deposition on aluminum are larger particle/substrate interfacial area and higher contact pressures. Both of these are the result of a larger kinetic energy associated with a heavier copper feed-powder particle.

The character of the dominant particle/substrate bonding mechanism is also discussed in the present paper. It is argued that an interfacial instability which can lead to the formation of interfacial roll-ups and vortices can play a significant role in attaining the high strength of interfacial bonding.

PACS: 81.05.Bx; 81.15.Rs

Keywords: Dynamic cold-spray process; Spray coating techniques

1. Introduction

Coatings are being increasingly used to obtain the required surface and tribological properties in engineering components. Such coatings are often applied using thermal-spray processes such as high velocity oxy-fuel, detonation gun, and plasma spray. In these processes, the coating material is heated to temperatures high enough to induce melting. Consequently, the high heat input to a part being coated accompanying these processes can be detrimental, if the material of the part degrades when subjected to high temperatures. This problem is generally avoided in the cold-gas dynamic-spray process. The cold-gas dynamic-spray process, often referred to as simply ''cold spray'', is a high-rate material deposition process in which fine, solid powder particles (generally 1–50 μm in diameter) are accelerated in a supersonic jet of

* Corresponding author. Tel.: +1-864-656-5639; fax: +1-864-656-4435.
E-mail address: mica.grujicic@ces.clemson.edu (M. Grujicic).

0169-4332/$ – see front matter © 2003 Elsevier Science B.V. All rights reserved.
doi:10.1016/S0169-4332(03)00643-3

Nomenclature

B	body force per unit mass
c	interfacial perturbation growth velocity
c_i	imaginary part of the interfacial perturbation growth velocity
D	rate of deformation
E	internal energy
EY	Young's modulus
J	Yih's function [19]
L	characteristic length scale
P	pressure
$\dot{Q}$	mass energy density source
Re	Reynolds number
S	deviatoric stress
t	time
T	temperature
U	characteristic velocity
υ	velocity
W	spin tensor
Y	yield strength

Greek letters

α	wave vector
$\dot{\varepsilon}$	total deviatoric deformation rate
$\dot{\varepsilon}^e$	elastic deviatoric deformation rate
$\dot{\varepsilon}^p$	plastic deviatoric deformation rate
Δt	time increment
Γ	Grüneisen function
η	amplitude of an interfacial perturbation
λ	instability wavelength
μ	viscosity
ν	kinematic viscosity
ρ	density
σ	stress
τ	interfacial perturbation growth time

Subscripts

R	reference curve
0	initial value
T	transpose

Superscripts

$'$	trial quantity
$\cdot$	time derivative

compressed (carrier) gas to velocities in a range between 500 and 1000 m/s. As the solid particles impact the target surface, they undergo plastic deformation and bond to the surface, rapidly building up a layer of deposited material. Cold spray as a coating technology was initially developed in the mid-1980s at the Institute for Theoretical and Applied Mechanics of the Siberian Division of the Russian Academy of Science in Novosibirsk [1,2]. The Russian scientists successfully deposited a wide range of pure metals, metallic alloys, polymers and composites onto a variety of substrate materials. In addition, they demonstrated that very high coating deposition rates on the order of 5 m^2/min ($\sim$300 ft^2/min) are attainable using the cold-spray process.

A simple schematic of a typical cold-spray apparatus is shown in Fig. 1. Compressed gas of an inlet pressure on the order of 3 MPa (500 psi) is introduced and flows through a converging/diverging nozzle to attain a supersonic velocity. The solid powder particles are metered into the gas flow upstream of the converging section of the nozzle and are accelerated by the rapidly expanding gas. To achieve higher gas flow velocities in the nozzle, the compressed gas is often preheated. However, while preheat temperatures as high as 900 K are sometimes used, due to the fact that the contact time of spray particles with the hot gas is quite short and that the gas rapidly cools as it expands in the diverging section of the nozzle, the temperature of the particles remains substantially below the initial gas preheat temperature and, hence, below the melting temperature of the feed-powder material.

Because the cold-spray process does not normally involve the use of a high-temperature heat source, it generally offers a number of advantages over the thermal-spray material deposition technologies. Among these advantages, the most important appear to be: (a) the amount of heat delivered to the coated part is relatively small so that microstructural changes in the substrate material are minimal or non-existent; (b) due to the absence of in-flight oxidation and other chemical reactions, thermally- and oxygen-sensitive depositing materials (e.g. copper or titanium) can be cold sprayed without significant material degradation; (c) nanophase, intermetallic and amorphous materials, which are not amenable to conventional thermal-spray processes (due to major degradation of the depositing material), can be cold sprayed; (d) grain growth and

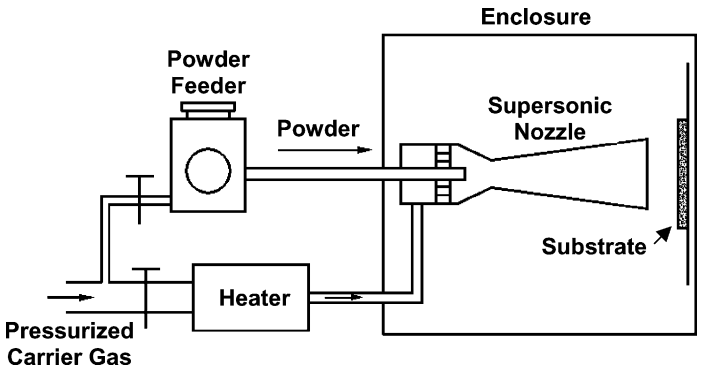

Fig. 1. Schematic of a typical cold-spray system.

formation of the embrittling phases are generally avoided; (e) macro- and microsegregations of the alloying elements during solidification that accompany conventional thermal-spray techniques, and can considerably compromise materials properties do not develop during cold spraying. Consequently, attractive feed-powder properties are retained in cold-sprayed bulk materials; (f) ''peening'' effect of the impinging solid particles can give rise to potentially beneficial compressive residual stresses in cold-spray deposited materials [3] in contrast to the highly detrimental tensile residual stresses induced by solidification shrinkage accompanying the conventional thermal-spray processes; and (g) cold spray of materials like copper, solder and polymeric coatings offers exciting new possibilities for cost-effective and environmentally-friendly alternatives to technologies such as electroplating, soldering and painting [4].

The actual mechanism by which the solid particles deform and bond during the cold-spray process is still not well understood. The most prevailing theory for cold-spray bonding postulates that, during impact, the solid particles undergo plastic deformation, disrupt thin (oxide) surface films and, in turn, achieve intimate conformal contact with the target surface. The intimate conformal contact combined with high contact pressures promotes bonding. This theory is supported by a number of experimental findings such as: (a) a wide range of ductile (metallic and polymeric) materials can be successfully cold-sprayed while non-ductile materials such as ceramics can be deposited only if they are co-cold-sprayed with a ductile (matrix) material; (b) the mean deposition particle velocity should exceed a minimum (material-dependent) critical velocity to achieve deposition which suggests that sufficient kinetic energy must be available to plastically deform the solid material and/or disrupt the surface film; and (c) the particle kinetic energy at impact is typically significantly lower than the energy required to melt the particle suggesting that the deposition mechanism is primarily, or perhaps entirely, a solid-state process. The lack of melting is directly confirmed through micrographic examination of the cold-sprayed materials [2].

Several research groups [5–8], have carried out comprehensive experimental studies to establish the effect of various process parameters such as: the type of the carrier gas, the gas preheat temperature, the average particle velocity, the particle impact angle, etc. on the deposition efficiency (defined as the mass percentage of the feed-powder particles deposited). The effect of these parameters can be considered as being well established and rationalized. However, the effect of the feed-powder particle and the substrate materials remains an outstanding issue. For instance, Gilmore and co-workers [8] (the results are reproduced in Fig. 2), found that the deposition of copper feed-powder particles on an aluminum substrate is associated with a significantly lower deposition-threshold particle velocity and a considerably higher value of the deposition efficiency in comparison to the deposition of aluminum-on-copper at a given average particle velocity. It should be noted that the data shown in Fig. 2 pertain to the initial deposition efficiencies, when copper particles are impacting the aluminum substrate in the case of copper deposition on aluminum and when aluminum particles are impacting the copper substrate in the case of aluminum deposition

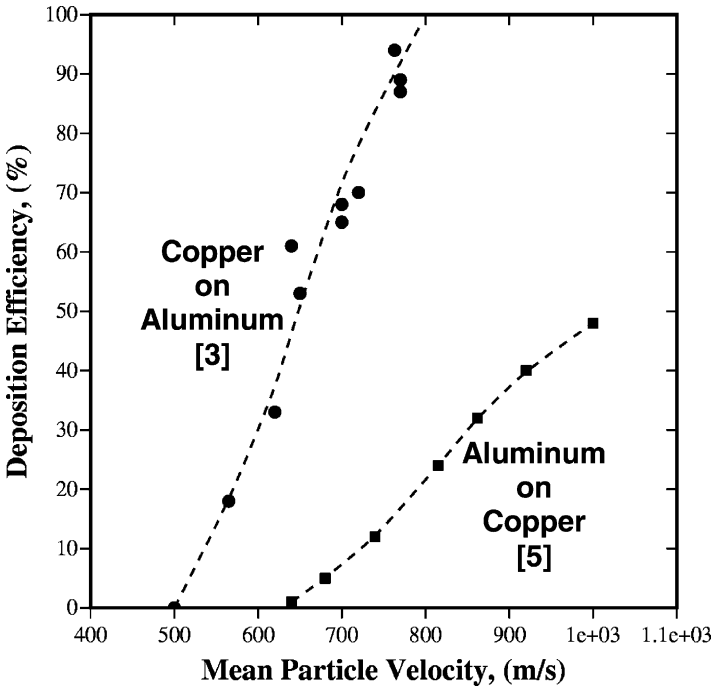

Fig. 2. Deposition efficiency as a function of the mean particle velocity for cold spraying of copper-on-aluminum and cold spraying of aluminum-on-copper [8].

on copper. Once, the substrate is covered with a one-particle thick layer of the coating material, further deposition takes place by the collisions of copper particles with the copper substrate and by the collisions of aluminum particles with the aluminum substrate. This later stage of the cold-spray deposition process will not be considered in the present work.

The objective of the present work is to carry out numerical simulations of the impact process of a single spherical feed-powder particle with a semi-infinite flat substrate in order to help elucidate the cold-spray particle/substrate bonding mechanism and the role of the particle and substrate materials. Toward that end, the computational method previously used by Dykhuizen et al. [9] is extended to study cold-spray deposition of copper-on-aluminum and aluminum-on-copper.

The organization of the paper is as follows: a brief overview of the equations governing the impact of a single feed-powder particle with a semi-infinite substrate is presented in Sections 2.1–2.3. Numerical solution of these equations using a finite-difference based method is discussed in Section 2.4. Details of the physical model used to study the impact of a particle with the substrate are overviewed in Section 3. The main results obtained in the present work are presented and discussed in Section 4. The key conclusions resulted from the present study are summarized in Section 4.

2. Computational procedure

All the simulations of the impact process of a single feed-powder particle with the substrate are carried out using the CTH computer code which was developed at the Sandia National Laboratory for modeling a wide range of solid dynamics problems involving shock wave propagation and material motion [10]. In this section, a brief description is given of the basic governing equations implemented in the CTH code and the numerical method used for obtaining the solution.

2.1. Conservation equations

Within the CTH code, the total stress tensor is decomposed into a hydrostatic (pressure), P, and a

deviatoric part, S. The evolution of the pressure, P, within each material, during an impact event is governed by an equation of state (e.g. $P = f(\rho, E)$, where ρ is the mass density, E the mass internal energy density, and f is used to denote a function). The deviation portion of the stress, S, within each material, is defined by a kinematic equation which combines a yield criterion, a flow rule and a material constitutive model.

Within the CTH code, the density, the velocity υ, and the internal energy density are defined by the following conservation equations:

- a mass conservation equation

$$\frac{\partial \rho}{\partial t} = -\rho \nabla \cdot \dot{\upsilon}, \tag{1}$$

- three momentum conservation equations

$$\rho \frac{\partial \upsilon}{\partial t} + \nabla \cdot (\sigma + IP) = -\rho B, \tag{2}$$

- and an energy conservation equation

$$\frac{\partial (\rho E)}{\partial t} = (\sigma + IP) \cdot \nabla \upsilon + \dot{Q} \tag{3}$$

These equations are solved in conjunction with an appropriate equation of state and a kinematics equation. In Eqs. (1)–(3), t is used to denote the time, I the second order identity tensor, B the body force per unit mass, and $\dot{Q}$ the mass energy density source term, while ∇ is used to denote the gradient and $\nabla\cdot$ the divergence operators and a dot atop a quantity to indicate a time derivative.

2.2. Equation of state

The relationships between P, E, ρ, and the temperature T are defined by the following Mie–Grüneisen equations of state [11]:

$$P(\rho, E) = P_{\mathrm{R}}(\rho) + \rho \Gamma (E - E_{\mathrm{R}}(\rho)), \tag{4}$$

and

$$E(\rho, T) = E_{\mathrm{R}}(\rho) + C_V (T - T_{\mathrm{R}}(\rho)), \tag{5}$$

where Γ is the Grüneisen function defined as $\Gamma = \rho^{-1}(\partial P/\partial E)_{\rho}$ and the subscript R is used to denote the quantities along a "reference curve," usually the Hugoniot, an isentrope, or the zero-Kelvin isotherm and $C_V = (\partial E/\partial T)_V$ is the constant-volume specific heat. These equations are most suitable at lower temperature, near the Hugoniot and do not account for phase transitions such as melting, vaporization, or chemical reactions and electronic excitation. The Hugoniot is represented by a quadratic relationship between the shock velocity υ_{s} and the particle velocity, υ_{p} as:

$$\upsilon_{\mathrm{s}} = C_S + S_1 \upsilon_{\mathrm{p}} + S_2 \frac{\upsilon_{\mathrm{p}}^2}{C_S} \tag{6}$$

where C_S is the speed of sound while S_1 and S_2 are material constants.

2.3. Materials constitutive equations

Two linear-elastic rate-dependent plastic material constitutive models, the Steinberg–Guinan–Lund (SGL) [12,13] and the Zerilli–Armstrong (ZA) model [14] both based on a consideration of thermally-activated and drag-controlled dislocation dynamics are used in the present work. Both models take into account the effects of isotropic strain-hardening, thermal softening, strain-rate-dependency and pressure-dependency of the yield strength, Y. In addition, the Steinberg–Guinan–Lund model accounts for the pressure- and temperature-dependency of the shear modulus, G.

Within the Steinberg–Guinan–Lund model [12,13], the yield strength is defined as:

$$Y = [Y_{\mathrm{T}}(\dot{\varepsilon}^{\mathrm{p}}, T) + Y_A f(\varepsilon^{\mathrm{p}})] \frac{G(P, T)}{G_0} \tag{7}$$

where the thermal component of the yield strength, Y_{T}, is defined by

$$\dot{\varepsilon}^{\mathrm{p}} = \left(\frac{1}{C_1} \exp \left[\frac{2U_K}{T} \left(1 - \frac{Y_{\mathrm{T}}}{Y_P} \right)^2 \right] + \frac{C_2}{Y_{\mathrm{T}}} \right)^{-1} \tag{8}$$

the function $f(\varepsilon^{\mathrm{p}})$ as:

$$f(\varepsilon^{\mathrm{p}}) = [1 + \beta(\varepsilon^{\mathrm{p}} + \varepsilon_i)]^n \tag{9}$$

and the shear modulus as:

$$G(P, T) = G_0 \left[1 + A \frac{P}{\eta^{1/3}} - B(T - 0.02585\,\mathrm{eV}) \right] \tag{10}$$

where $Y_A, C_0, C_1, C_2, U_K, Y_P, \beta, \varepsilon_i, n, A$ and B are material-dependent parameters, ε^{p} the equivalent

plastic strain, $\dot{\varepsilon}^{\mathrm{p}}$ the equivalent plastic strain rate and $\eta \equiv \rho/\rho_0$ the compression and ρ_0 the initial density. The temperature T is expressed in eV and is defined as kT^*, where k is the Boltzmann's constant and T^* is the temperature in degrees of Kelvin.

Within the Zerilli–Armstrong model [14], the yield strength is defined as:

$$Y = A' + (c_1 + c_2\sqrt{\varepsilon^{\mathrm{p}}})\mathrm{e}^{-c_3 T}(\dot{\varepsilon}^{\mathrm{p}})^{c_4 T} + c_5(\varepsilon^{\mathrm{p}})^N \qquad (11)$$

where $A', c_1, c_2, c_3, c_4, c_5$ and N are material-dependent parameters.

When a cell contains two or more materials, the yield strength is defined as the volume fraction weighted yield strength of the individual materials. Consequently, single material cells containing voids have a reduced yield strength since the material volume fraction in such cells is less than unity.

2.4. Yield criterion and flow rule

The von Mises yield criterion is implemented into the CTH code according to which (plastic) yielding occurs when the magnitude of the deviatoric stress, $|S| = \sqrt{S \cdot S}$ (a raised dot is used to denote the tensor inner product) reaches (or exceeds) a material-state, temperature and loading-rate-dependent value of

$$|S| = \sqrt{\tfrac{2}{3}}Y \qquad (12)$$

where the yield strength Y is given by either Eqs. (7) or (11). Upon yielding an *associated* flow rule is used to describe the subsequent plastic deformation. According to this flow rule, plastic flow occurs in such a way to most rapidly accommodate the deviatoric part of the stress which causes the plastic flow and, hence, the (deviatoric) plastic strain rate, $\dot{\varepsilon}^{\mathrm{p}}$, is defined as:

$$\dot{\varepsilon}^{\mathrm{p}} = |\dot{\varepsilon}^{\mathrm{p}}|\frac{S}{|S|} \qquad (13)$$

where $||$ is used to denote the magnitude of a tensor. The total deviatoric strain rate, $\dot{\varepsilon}$, is defined as:

$$\dot{\varepsilon} = D - \tfrac{1}{3}\,\mathrm{tr}(D)I \qquad (14)$$

where D, given as:

$$D = \tfrac{1}{2}(\nabla\upsilon + \nabla\upsilon^{\mathrm{T}}) \qquad (15)$$

is the rate of deformation tensor, I the identity tensor, superscript T denotes the tensor transpose, and tr the tensor trace. The total deviatoric strain rate $\dot{\varepsilon}$ can be additively decomposed into its elastic, $\dot{\varepsilon}^{\mathrm{e}}$, and plastic, $\dot{\varepsilon}^{\mathrm{p}}$, components as:

$$\dot{\varepsilon} = \dot{\varepsilon}^{\mathrm{e}} + \dot{\varepsilon}^{\mathrm{p}} \qquad (16)$$

The elastic deviatoric strain rate is assumed to be governed by Hooke's law and can be defined as:

$$\dot{\varepsilon}^{\mathrm{e}} = \frac{1}{2G}(\dot{S} - WS + SW) \qquad (17)$$

where the quantity within parentheses is known as the Jaumann co-rotational stress rate and

$$W = \tfrac{1}{2}(\nabla\upsilon - \nabla\upsilon^{\mathrm{T}}) \qquad (18)$$

is the spin tensor.

The evolution of the deviatoric stress, S, between the times t and $t + \Delta t$, where Δt is a time increment, can be generally expressed using a backward Euler scheme as:

$$S_{t+\Delta t} = S_t + \dot{S}_{t+\Delta t}\,\Delta t \qquad (19)$$

where $\dot{S}$ is defined by inverting Eq. (17) as:

$$\dot{S} = 2G\dot{\varepsilon}^{\mathrm{e}} + WS - SW \qquad (20)$$

The deviatoric stress at the end of a time step $t = \Delta t$, $S_{t+\Delta t}$, is updated within the CTH code using the radial return procedure developed by Kreig and Kreig [15], which uses the total deviatoric strain rate in place of the elastic deviatoric strain rate to obtain a trial deviatoric stress, $S_{t+\Delta t}{}'$, as:

$$S_{t+\Delta t}{}' = S_t{}' + 2G\dot{\varepsilon}\,\Delta t \qquad (21)$$

The magnitude of the trial deviatoric stress is next relaxed to account for the effect of plasticity in accordance with the yield criterion, Eq. (12), as:

$$|S_{t+\Delta t}| = |S_{t+\Delta t}{}'| - 2G|\dot{\varepsilon}^{\mathrm{p}}|\,\Delta t = \sqrt{\tfrac{2}{3}}Y_{t+\Delta t} \qquad (22)$$

Since, the shear modulus is a function of T and P, Eq. (10), the total strain rate a function of υ, Eqs. (14) and (15), and the yield strength is a function of P, T, $|\varepsilon^{\mathrm{p}}|$, and $|\dot{\varepsilon}^{\mathrm{p}}|$, Eqs. (7) and (11), Eq. (22) can be written in a general form as:

$$S_{t+\Delta t}(\upsilon, T, P, |\dot{\varepsilon}^{\mathrm{p}}|) = \sqrt{\tfrac{2}{3}}Y_{t+\Delta t}(P, T, |\bar{\varepsilon}^{\mathrm{p}}|, |\dot{\varepsilon}^{\mathrm{p}}|) \qquad (23)$$

and can be considered as the governing equation for the magnitude of the (deviatoric) plastic strain rate, $|\dot{\varepsilon}^{\mathrm{p}}|$.

Once $|\dot{\varepsilon}^{p}|$ is computed, the deviatoric plastic strain rate is determined using Eq. (13), then the deviatoric elastic strain rate computed using Eq. (16), and finally, the deviatoric stress updated as:

$$S_{t+\Delta t} = S_t' + 2G\dot{\varepsilon}^{e}\,\Delta t \tag{24}$$

Thus, Eq. (24) in conjunction with Eqs. (12)–(23) can be considered as the governing equations for the evolution of the deviatoric stress, S.

2.5. Numerical solution

Eqs. (1)–(5), (7) or (11), (10), (22) and (24), define a system of nine coupled partial differential and algebraic equations with the time t and the spatial coordinates x, y, and z as independent variables and ρ, υ, E, P, T, Y, G, S, and ε^{p} as nine dependent variables. After assigning the initial and boundary conditions for the dependent variables, the coupled system of partial and algebraic equations is numerically solved within the CTH code using a finite-difference based two-step Eulerian computational scheme. In the first step, the Lagrangian step, the computational mesh is attached to the material and, hence, the cells distort in order to follow the material. In the second step, the Eulerian step, remeshing is carried out in order to map the distorted cells back to the original Eulerian mesh.

3. Modeling of the particle/substrate impact process

While the angle at which feed-powder particles impact the substrate is known to affect the deposition efficiency (e.g. [8]), all the simulations carried out in the present work deal with normal-angle impacts. This was done for the two main reasons: (a) normal-angle impacts enable the use of an axisymmetric geometry avoiding the need for computationally costly three-dimensional simulations; and (b) the main objective of the present work is to analyze the effects of feed-powder particles and substrate materials and the particle size, velocity and temperature on the deposition process and not the effect of the angle of impact.

The substrate is modeled as a semi-infinite 200 μm-diameter cylinder, while a 20 μm-diameter sphere is used to represent the feed-powder particle. The following two combinations of the particle/substrate materials are studied: (a) copper/aluminum; and (b) aluminum/copper. These two combinations of the particle/substrate materials are considered, in order to help explain the experimental results displayed in Fig. 2 which show that the cold-spray deposition efficiency is substantially higher for copper deposited on aluminum than the vice versa.

As discussed in Section 2.3, two types of elastic rate-dependent plastic materials constitutive models are considered in the present work: (a) the Steinberg–Guinan–Lund [12,13] and the Zerilli–Armstrong [14] models. The CTH materials database for the Steinberg–Guinan–Lund model contains all the parameters, except for the strain-rate parameters, for copper and 1100-O-aluminum. The strain-rate dependence parameters for the Zerilli–Armstrong model are available within the CTH materials database. Unfortunately, currently this database contains the Zerilli–Armstrong model parameters only for copper. Hence, in order to assess the effect of strain-rate-dependency of yield strength on the particle/substrate impact, the following particle/substrate materials models have been considered: (a) SGL–copper/SGL–aluminum (no effect of strain rate accounted for); (b) SGL–aluminum/SGL–copper (no effect of strain rate account for); (c) ZA–copper/SGL–aluminum (the strain-rate effect account for only in copper particles); and (d) SGL–aluminum/ZA–copper (the effect of stain rate accounted for only in the copper substrate). Only the results pertaining to the cases (c) and (d) are presented in this paper since they are qualitatively quite similar to and quantitatively within a few percent of their counterparts for the cases (a) and (b). The SGL and the ZA materials constitutive model parameters and the Mie–Grüneisen equation of state parameters for commercially-pure copper and 1100-O-aluminum used in the present work can not be reported here since their dissemination is prohibited by the US Department of State International Traffic and Arms Regulations, 22CFR120-130.

All the calculations are carried out assuming that the feed-powder particle and the substrate are initially at room temperature while different particle velocities within the range 400–1000 m/s are considered.

The computational domain containing a single feed-powder particle and the substrate is discretized using a mesh consisting of quadrilateral cells. To ensure a fine cell size in the particle/substrate contact

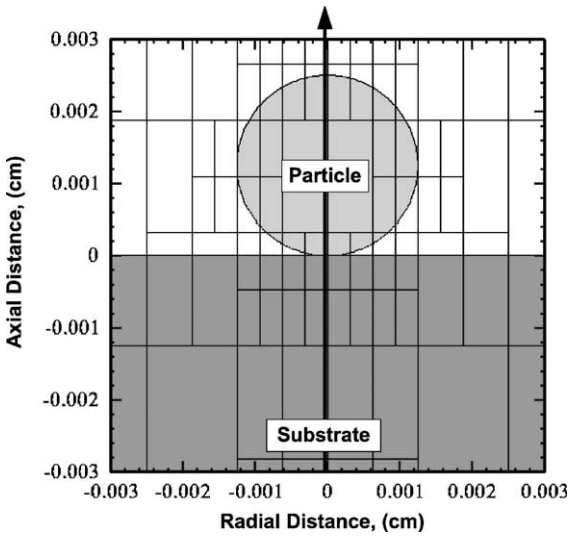

Fig. 3. The computational domain and the hierarchical block structure used in the numerical simulation of the particle/substrate impact.

region, an adaptive mesh refinement strategy implemented in the CTH code is used. This strategy is block-based, with the blocks (each containing the same number of cells) connected in a hierarchal manner with the adjacent ones and with a maximum cell-size ratio limited to 2:1. An example of the hierarchal block structure is displayed in Fig. 3. The interfacial high-resolution region of the mesh is created by splitting blocks midway along each of the coordinate directions. This produces four child blocks per parent block for a two-dimensional problem. Likewise, four blocks are recombined to form a single block when such blocks are located far away from the particle/substrate interface.

A symmetry boundary condition is used along the vertical axis of the particle/substrate assembly, Fig. 3. Sound speed based absorbing (transmitting) boundary conditions are used along the bottom and the side surfaces of the substrate. These boundary conditions allow a mass flow into and out of the computational domain and are generally used to approximate an

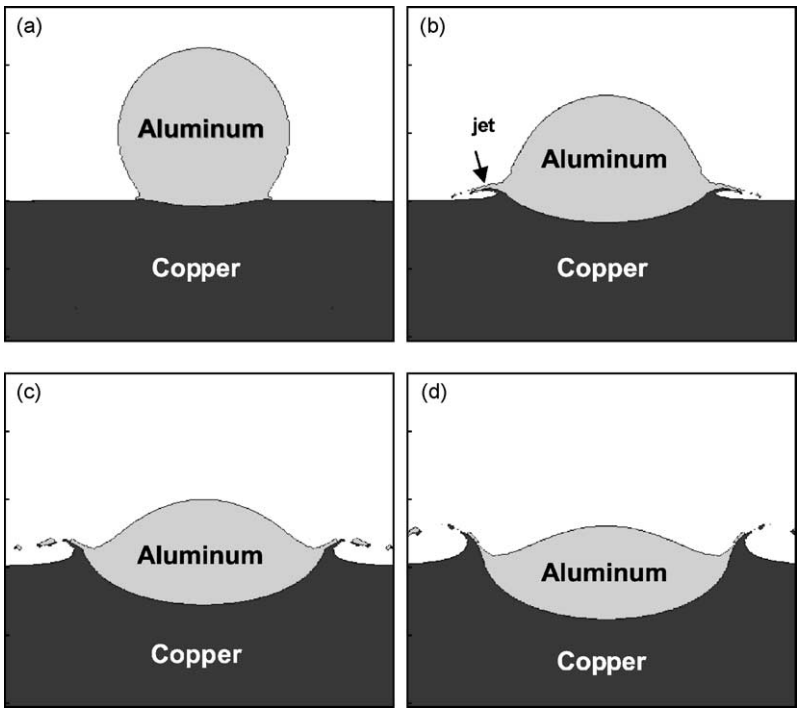

Fig. 4. The evolutions of shapes of a 20 μm-diameter aluminum feed-powder particle and a copper substrate-crater for the incident particle velocity of 650 m/s at the times: (a) 5 ns; (b) 20 ns; (c) 35 ns; and (d) 50 ns.

infinite or a semi-infinite medium. Along the remaining portion of the computational domain, the pressure is set to zero within the ''ghost'' cells (the cells with the void volume fraction equal to unity). The use of this boundary condition prevents the mass from entering the computational domain while a mass flow out of the computational domain is allowed.

4. Results and discussion

4.1. The evolutions of shapes of the particle and the substrate-crater

The simulation results of the collision between a single 20 μm-diameter aluminum particle with the incident velocity of 650 m/s and a flat semi-infinite copper substrate at four times (5, 20, 35 and 50 ns) following the initial particle/substrate contact are shown in Fig. 4(a)–(d), respectively. According to Fig. 2, 650 m/s is slightly above the minimum critical incident particle velocity for aluminum cold-spray deposition onto a copper substrate. The results displayed in Fig. 4(a)–(d) show that as the particle/substrate contact time increases, the particle (height-to-width) aspect ratio decreases while the substrate-crater depth and width increase. At the same time, a jet composed of both the particle material and the substrate material is formed at the particle/substrate contact surface. When this jet reaches the free surface, it forms a lip which points away from the flattened particle. Fracture of the material at the jet front as seen in Fig. 4(b)–(d) is controlled by a hydrostatic tensile stress condition and, since it is not the focus of the present work, will not be discussed any further.

The evolutions of shapes of a single 20 μm-diameter copper particle with an incident velocity of 650 m/s and a flat semi-infinite aluminum substrate at the same four times as in Fig. 4(a)–(d) are shown in Fig. 5(a)–(d), respectively. According to Fig. 2, the deposition efficiency of copper-on-aluminum substrate at an incident particle velocity of 650 m/s is ~50–60%. The results displayed in Fig. 5(a)–(d) show, like the results displayed in Fig. 4(a)–(d), that

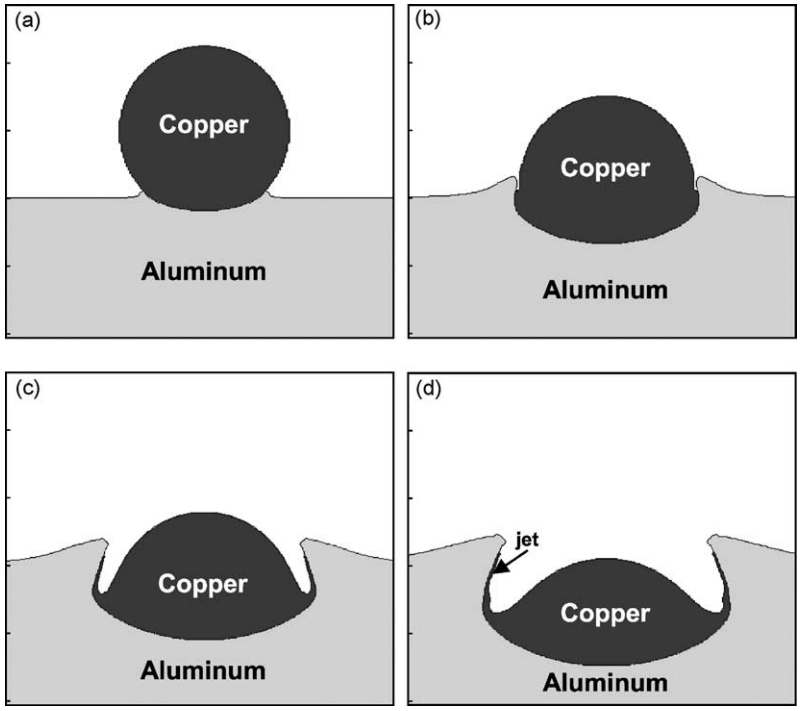

Fig. 5. The evolutions of shapes of a 20 μm-diameter copper feed-powder particle and a aluminum substrate-crater for the incident particle velocity of 650 m/s at the times: (a) 5 ns; (b) 20 ns; (c) 35 ns; and (d) 50 ns.

as the particle/substrate contact time increases, the crater depth and width increase while the flattened particle aspect ratio decreases. However, in this case, the crater is much deeper and, due to the fact that the particle is flattened to a lesser extent, the crater width and the final particle/substrate contact surface area (excluding the one associated with the interfacial jet) are somewhat smaller. These differences can be attributed to the larger kinetic energy associated with the heavier copper feed-powder particle and to the larger strength of copper in comparison to that of aluminum. One of the most striking differences between the corresponding results shown in Figs. 4(a)–(d) and 5(a)–(d) is in the length of the interfacial jets. The interfacial jet is much longer in the case of the copper deposition on aluminum than in the case of the aluminum deposition on copper.

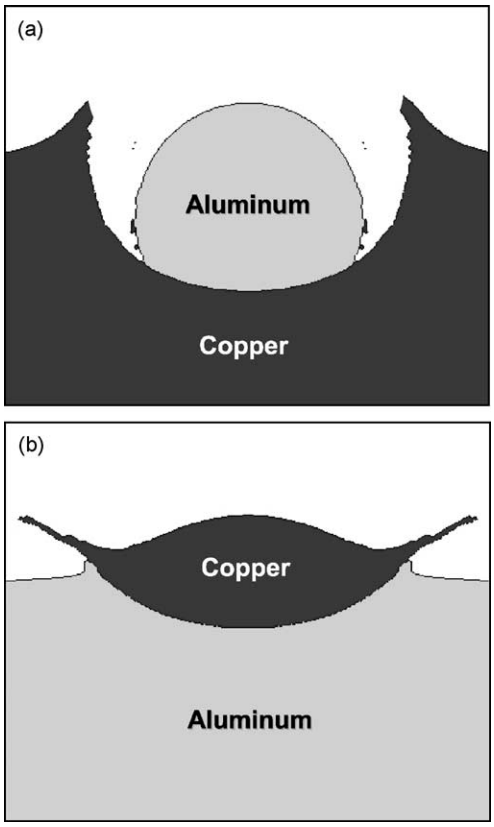

Fig. 6. The shapes of the feed-powder particle and the substrate-crater 50 ns following the initial contact for: (a) the aluminum particle velocity of 400 m/s; and (b) copper particle velocity of 500 m/s.

The shapes of the feed-powder particles and the substrate-craters 50 ns following the initial contact for the aluminum particle velocity of 400 m/s and the copper particle velocity of 500 m/s are shown in Fig. 6(a)–(b), respectively. These two velocities are lower than the corresponding minimum critical particle velocity for cold-spray deposition. By comparing the results displayed in Fig. 6(a)–(b) with the ones displayed in Figs. 4(a)–(d) and 5(a)–(d) one can observe that the interfacial jet is composed of only one material at the sub-critical particle velocities. This finding suggests that the role of the interfacial jets in removing the oxides and other surface films from both the particle surface and the substrate surface is a critical factor for attaining a good particle/substrate bonding (i.e. a high level of deposition efficiency).

The time evolutions of the maximum temperature, the maximum plastic strain rate, the maximum pressure, and the maximum von Mises equivalent stress, all at the aluminum particle/copper–substrate interface at the incident particle velocity of 400, 600, 800 and 1000 m/s are shown in Fig. 7(a)–(d), respectively. The corresponding results for the copper cold-spray deposition onto an aluminum substrate are shown in Fig. 8(a)–(d).

The results depicted in Figs. 7(a) and 8(a) show that the maximum temperature at the particle/substrate interface briefly (for ∼11 ns in the copper-on-aluminum case and for ∼20 ns in the copper-on-aluminum case) exceeds the melting point of aluminum (∼940 K) and only at the highest incident particle velocities (1000 m/s) used. The melting point of copper (∼1356 K) is never exceeded. It should be noted that the computed maximum temperature values at the particle/substrate interface are overestimated due to the fact that the CTH code does not enable modeling of the transfer of heat from the particle/substrate interface region where the heat is generated. A close examination of the temperature distribution over the particle/substrate interface shows that the conditions for melting of the aluminum particle or substrate are met over a very small portion of the interface (approximately 14 and 20% of the particle/substrate interfacial area in the aluminum-on-copper and the copper-on-aluminum cases, respectively). Also, the heat-diffusion distance in the copper particle or the substrate during a typical collision time period of 50 ns is about 3–4 μm suggesting that heat conduction can play a

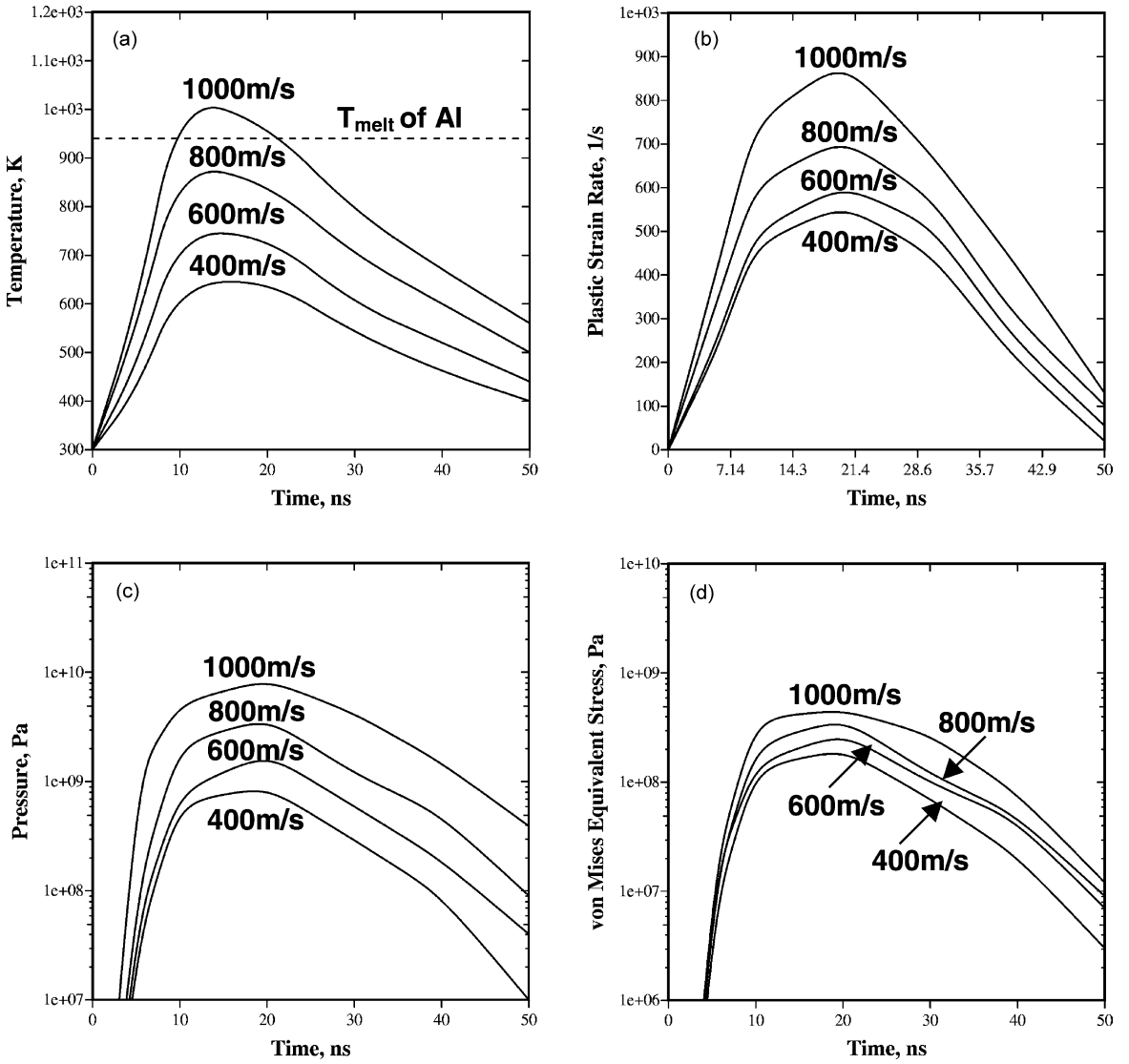

Fig. 7. The evolutions of the maximum: (a) temperature; (b) plastic strain rate; (c) pressure; and (d) von Mises equivalent stress at the particle/substrate interface during the deposition of aluminum-on-copper at four particle velocities.

significant role in reducing the maximum interfacial temperature during the particle/substrate collision process. These findings suggest that melting, even if it takes place, most likely does not play a key role in particle/substrate bonding. This is fully consistent with numerous metallographic examination results which generally show a cold-worked grain structure in the region surrounding the particle/substrate interface in the systems with good particle/substrate bonding (e.g. [16]).

The results displayed in Figs. 7(b) and 8(b), as well as the ones depicted in Figs. 4(a)–(d) and 5(a)–(d), show that, due to a large impact velocity of the feed-powder particle with the substrate, the plastic deformation is highly localized for the region surrounding the particle/substrate interface. Consequently, a jet is formed which removes the oxidized and/or otherwise contaminated material from the prior particle and the substrate surfaces. Consequently, clean particle and substrate materials are brought into contact

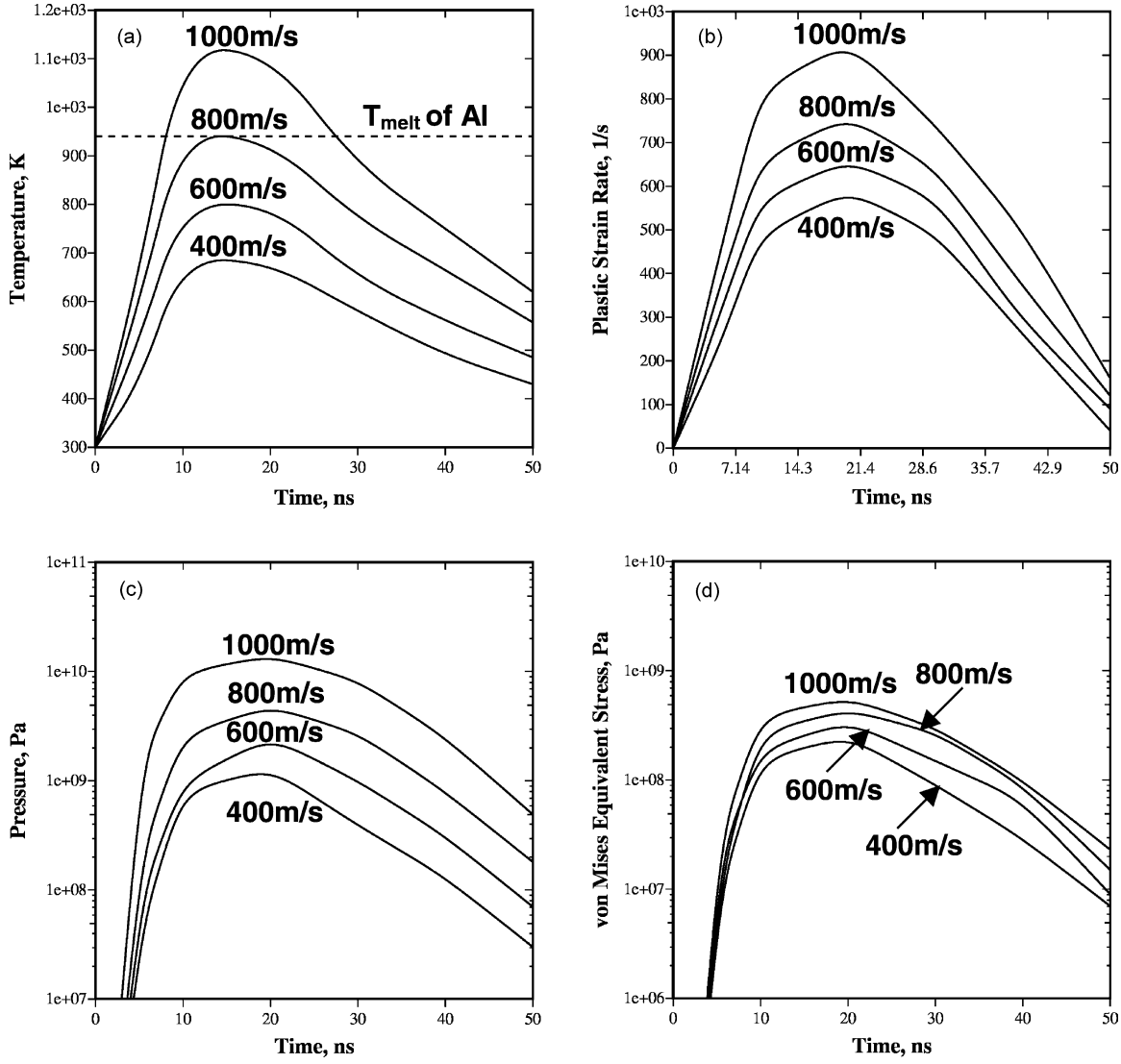

Fig. 8. The evolutions of the maximum: (a) temperature; (b) plastic strain rate; (c) pressure; and (d) von Mises equivalent stress at the particle/substrate interface during the deposition of copper-on-aluminum at four particle velocities.

(under high pressures) at the particle/substrate interface during the collision process. Formation of such jets and their role in removing the contaminated material from the particle and substrate surfaces is believed to be one of the major (necessary) conditions controlling the strength of particle/substrate bonding.

The results shown in Figs. 7(c)–(d) and 8(c)–(d), show that, for both aluminum deposition on copper and copper deposition on aluminum, the contact pressure and the von Mises equivalent stress values (the latter is numerically equal to the material yield strength) are very high in comparison to the yield strength in the un-deformed ($\varepsilon^{p} = 0$) constituent materials at the maximum interfacial particle/substrate interface temperatures and plastic strain rates. For example, for the case of aluminum deposition on copper at the particle velocity of 800 m/s, at the maximum interfacial temperature (~870 K) and at the maximum plastic strain rate (~660 s^{-1}), zero plastic strain yield strengths of aluminum and copper are 0.3×10^{8} Pa and

0.8×10^8 Pa, respectively. The corresponding maximum interfacial pressures and the maximum interfacial von Mises equivalent stress ($\sim 4.1 \times 10^9$ Pa and $\sim 3.8 \times 10^8$ Pa, respectively) are, thus, higher than the zero plastic strain yield strengths of the two constituent materials by a factor between 5 and 130. This finding suggests that, due to these extremely high pressure and stress levels, it may be perhaps more appropriate to treat the material adjacent to the particle/matrix interface as a viscous "fluid-like" material rather than a rate-dependent elastic–plastic solid material. Such a suggestion was previously made in the context of explosive welding (e.g. [17]), using the same argument as the one presented above. By defining the viscosity, μ, as the proportionality constant between the equivalent shear stress and the equivalent shear rate, the viscosity of copper and aluminum under the deposition conditions modeled in the present work is estimated, using Eqs. (7) and (11), to be between 10^5 and 10^6 P. Once, the material surrounding the particle/substrate interface is assumed to be a viscous material, one can proceed to investigate the potential effect of various fluid-based phenomena such as interfacial instabilities and the resulting interfacial waves, roll-ups and vortices on the strength of particle/substrate bonding. The potential role that such instabilities may play in particle/substrate bonding is discussed in Section 4.3.

4.2. Interfacial bonding mechanisms

Many experimental and theoretical/computational investigations, including the present one, have documented the formation of "surface-scrubbing" jets, high interfacial pressures, large extents of plastic deformation in the interfacial region and the associated increases in temperature. However, a generally acceptable explanation for the dominant mechanism for particle/substrate bonding is still lacking. As discussed earlier, interfacial melting may occur and enhance the particle/substrate interfacial bonding but it is not believed to be a major factor controlling the bonding strength. Formation of the "surface-scrubbing" jets and high contact pressures are generally considered as prerequisites for good particle/substrate bonding. However, these factors, while critical for attaining clean particle and substrate surfaces and an intimate contact between them, do not, per se, offer any insight into the character of the dominant mechanism or mechanisms of interfacial bonding under the dynamic cold-spray conditions.

The most frequently cited particle/bonding mechanisms under the dynamic cold-spray conditions are atomic diffusion, surface adhesion and plastic deformation. In the following, simple semi-quantitative arguments are used to examine the potential role of these three bonding mechanisms.

Using the Al–Cu inter-diffusion coefficient, $D_{\text{cu–Al}}$ ($=10^{-15}$ to 10^{-14} m^2/s [18]), the atomic inter-diffusion distance, during the time period of $\sim$20 ns over which the particle/substrate interface is subjected to the highest temperatures, is found to be only 0.004–0.1 nm (i.e. a fraction of the inter-atomic distance). This finding suggests that the atomic diffusion at the particle/substrate interface may be excluded as a dominant particle/substrate bonding mechanisms under the dynamic cold-spray deposition conditions.

Adhesion is an atomic length-scale phenomenon and its occurrence is controlled by the presence of clean surfaces and high contact pressures to make the two surfaces mutually conforming. The strength of adhesion then depends on the (attractive or repulsive) character of atomic interactions and the crystallographic details of the interface. While adhesion can be modeled using atomic-scale simulations, such a study is beyond the scope of the present work. Nevertheless, one can generally infer the character of atomic interaction by examining the corresponding binary phase diagram. Specifically, the existence of a solubility limit is an indication of repulsive atomic interactions, while the formation of an intermediate/intermetallic compound is an indication of attractive atomic interactions. Complete mutual solubility of two metals indicates weak repulsive or attractive atomic interactions. In addition to the factors discussed above, the overall strength of adhesion-based particle/substrate bonding depends on the size of the particle/substrate interfacial area. It is generally observed that stronger bonding occurs when the interfaces are wavy and when it contains vortex-like features (e.g. [17]). This observation can be, at least partly, attributed to the associated increase in the interfacial area. However, as discussed in the context of explosive welding (e.g. [17]), interfacial perturbations (roll-ups and vortices) can give rise to nano/microscale material mixing and mechanical

interlocking, both of which enhance the interfacial bonding. A more detailed discussion of these interfacial instability-based phenomena is presented in the next section. For now, the experimentally observed stronger bonding (i.e. a higher deposition efficiency) in the case of copper deposition on aluminum than that for the aluminum deposition on copper can be tentatively attributed to the effect of higher contact pressures and a more effective scrubbing effect of the interfacial jet, both of which increase the overall strength of adhesion-based interfacial bonding.

Plastic deformation is generally considered to be a mechanism for energy dissipation, i.e. a source of heat in the interfacial region. However, as shown earlier, increased temperature in the interfacial region, is not sufficient to enhance interfacial melting or atomic diffusion to a level at which they act as dominant interfacial bonding mechanisms.

4.3. The role of interfacial instability

The discussion presented in the previous paragraphs suggests that, considering the very short times during which the particle/substrate is subjected to high temperatures and high pressures, the experimentally observed good interfacial bonding at the particle velocities exceeding a critical incident particle velocity, is most likely the result of some type of nano/microlength-scale mechanical material mixing/interlocking mechanism. In the following, two interfacial instability-based mechanisms are suggested by which such mixing/interlocking may occur.

Interfacial instability and the resulting formation of interfacial roll-ups and vortices can be, perhaps, best understood within the context of the Kelvin–Helmholtz instability phenomenon. This phenomenon can arise when two fluids, in contact, are moving at different velocities in a direction parallel to their interface. Instability can occur even if the two fluids have identical densities. When the interface is subjected to a (non-zero curvature) perturbation, then as one fluid flows around the other a centrifugal force is generated. This, in turn, gives rise to a change in pressure which may promote amplification of the interfacial perturbation. As shown schematically in Fig. 9, these instabilities may subsequently lead to the formation of interfacial roll-ups and vortices. Such interfacial roll-ups and vortices may enhance the overall strength of interfacial bonding by at least three ways: (a) by significantly increasing the interfacial area available for adhesion; (b) by producing a fine length-scale mixing of the two material; and (c) by creating mechanical interlocking between the two materials.

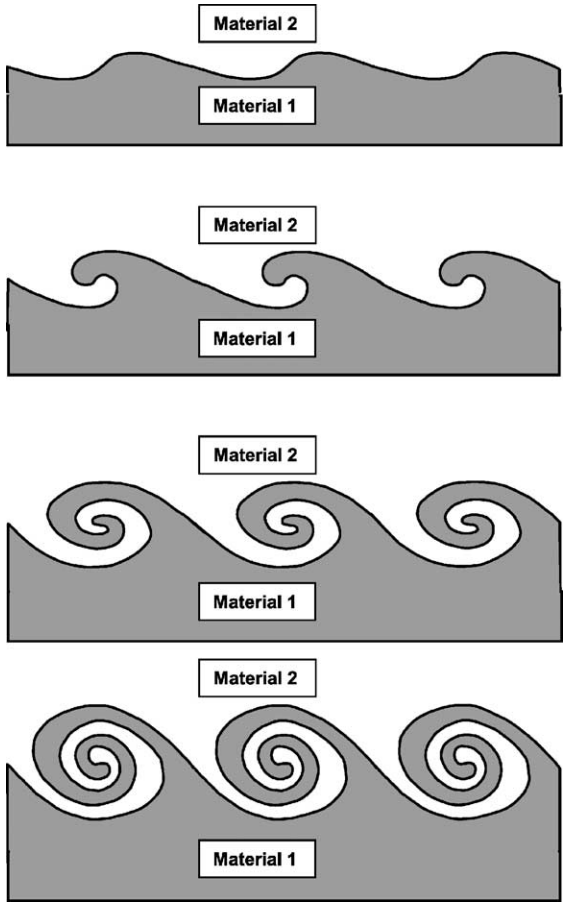

Fig. 9. A schematic of the instability-based evolution of the particle/substrate (Material 1/Materia 2) interface and the accompanying formation of interfacial roll-ups and vortices.

Interfacial instabilities are typically understood within the context of inertial instabilities, where flow inertia acts to promote the instability and viscosity acts to dampen it. The ratio of these two effects determines if the instability actually grows or decays and is quantified by the Reynolds number as:

$$Re = \frac{UL}{v} \tag{25}$$

where U is the characteristic velocity, L is the characteristic length scale, and $v\,(=\mu/\rho)$ is the kinematic viscosity. For the situation considered here, a characteristic velocity would be the particle impact velocity which is on the order of 1000 m/s, and a characteristic length scale would be the particle diameter which is on the order of 10 μm. The values of μ cited earlier range from 10^5 to 10^6 P, which translate to kinematic viscosities of ~100 m^2/s assuming a metal density on the order of 1000 kg/m^3. Using these numbers, a value of $Re \sim 10^{-4}$ is obtained. Since instabilities arise when the Reynolds number is substantially larger than one, inertial instability is not expected to occur in the present situation, the rather rough estimates of length, velocity and kinematic viscosity notwithstanding.

On the other hand, the work of Yih [19] has demonstrated that an interfacial instability based on viscosity differences between the two flowing streams may occur, even for vanishing Reynolds number. The governing equations for this viscous instability are quite complex and their detailed analysis is beyond the scope of the present work. Instead, a brief overview of the key equations is presented to illustrate the feasibility of this instability and its potential role as a particle/substrate bonding mechanism. Following the analysis of Yih [19], the amplitude of an interfacial perturbation η is described by the equation:

$$\eta \sim e^{i\alpha(x'+ct)} \tag{26}$$

where x' is position along the interface, $\alpha = 2\pi/\lambda$ the wave vector, and λ and c the wavelength and the growth velocity of the perturbation. Accordingly, the interface becomes unstable when the imaginary part of the perturbation velocity c, c_i is positive and grows at a rate which is proportional to the magnitude of c_i. Yih [19] developed the following equation for the imaginary part of the perturbation velocity:

$$c_i = \alpha ReJ \tag{27}$$

where J is a function of several variables and is given by Eq. (42) in reference [19]. The magnitude of J is generally of the order of 10^4 to 10^5 m^2/s. According to Eq. (26), the amplitude of an unstable perturbation increases by a factor of e over a time period of $\tau \sim 1/\alpha c_i$. After substituting c_i from Eq. (27), this time period can be expressed as:

$$\tau = \frac{1}{\alpha^2 ReJ} \tag{28}$$

The analysis presented above enables one to ascertain whether a perturbation with the wavelength comparable to that of experimentally observed waves (ripples) along the particle/substrate interface will grow at a rate high enough to form roll-ups and vortices during the time scale of the particle/substrate collision event. For example, taking a wavelength of 1 μm (smaller than the particle size by more than an order of magnitude), and using the value of the Reynolds number of 10^{-4} obtained earlier and a value of $J = 10^4$ to 10^5 m^2/s yields a time period over which an unstable perturbation undergoes a significant growth of $\tau \sim 10^{-14}$ to 10^{-15} s. Typical particle/substrate collision times are on the order of tens of nanoseconds, indicating that a 1 μm-wavelength perturbation is unstable and would grow during a collision event. Furthermore, Eq. (28) reveals that perturbations with smaller wavelengths (larger wave vectors) will grow even more rapidly, suggesting that this type of instability can be expected to result in the formation of interfacial roll-ups and vortices. Since heavier copper particles are associated with larger kinetic energies, their collisions with the substrate are expected to give rise to formation of the interfacial perturbations with smaller wavelengths in the case of copper deposition on aluminum relative to those encountered in the aluminum-on-copper deposition case. This may be one of the reasons for the experimentally observed higher deposition efficiencies in the case of copper deposition on aluminum.

The Yih interfacial instability analysis [19] presented above can further be used to rationalize the experimentally observed stronger bonding of copper-on-aluminum than that for aluminum-on-copper. Fig. 2(a) in reference [19] shows that the magnitude of the function J is dependent on the viscosity ratio $m = \mu_1\mu_2$ and on the thickness ratio of the two fluid streams, $n = h_1/h_2$, where subscripts 1 and 2 are used to denote the streams with a lower and a higher thickness, respectively. For the case of aluminum deposition on copper, Fig. 4(c) suggests that a thinner jet is associated with the aluminum particle, and n has been estimated as 0.8–1.0. Using the procedure described in Section 4.1, the aluminum viscosity to copper viscosity ratio m has been evaluated as 0.5–1.0. Based on Fig. 2(a) in reference [19] the corresponding magnitude of the J function is assessed as $(0.5-1.0)\times 10^4$ m^2/s. For the case of copper deposition on

aluminum, Fig. 5(d) suggests that a thinner jet is associated with the copper particle, and n has been estimated as 0.1–0.3. The copper viscosity to aluminum viscosity ratio m is 1.0–2.0. Based on Fig. 2(a) in reference [19] the corresponding magnitude of the J function is assessed as $(1.0-3.0) \times 10^5$ m^2/s. According to Eq. (28) and these estimates for J, the growth velocity of interfacial perturbations is expected to be larger, by at least an order of magnitude, for the copper-on-aluminum deposition case relative to that for the aluminum-on-copper deposition case. Thus, the role of interfacial instability in promoting particle/substrate bonding is expected to be more pronounced in the case of copper-on-aluminum deposition and is another potential reason for the observed higher deposition efficiency. While a detailed microstructural investigation of the differences in interfacial morphologies in the two cases under consideration is currently lacking, a careful examination of the scanning and transmission electron micrographs in references [3,5], seem to indicate that the extent of interfacial perturbations is somewhat larger in the case of copper deposited on aluminum than in the case of aluminum deposition on copper. One must, however, recognize that due to high temperatures attained during the particle/substrate collision process, the microstructure in the interfacial region is generally altered by recrystallization. Hence, experimental validation of the proposed interfacial bonding mechanism should include, in addition to a high-resolution microstructural investigation, a chemical analysis at the same length scale.

Finally, in addition to, or instead of the interfacial instability mechanism described above, a simpler topological bonding mechanism is also suggested. Fig. 5 shows the evolution of the particle and the substrate-crater shapes during an impact event when the particle is copper and the substrate is composed of aluminum. A particularly important feature to note in this figure is that the cavity formed by the impact is reentrant, and that the copper particle completely conforms to the boundaries of this reentrant cavity. This is important because such a cavity, once formed, prevents the copper material from being separated from the aluminum substrate. For example, even if the two materials do not adhere firmly to each other, such a topological geometry would prevent separation of the materials due to the rivet-like nature of the interface. If such a shape were observed only when deposition efficiencies were greater than zero, and was absent when deposition efficiencies were equal to zero, then the presence of this rivet-like shape might be the feature which controls the bonding process. To further explore this idea, the topologies of the two material systems under conditions where their deposition efficiencies are exactly zero are reviewed. These situations are illustrated in Fig. 6(b) for the copper-on-aluminum system and in Fig. 4(d) for the aluminum-on-copper system. In spite of the different impact velocities, the impact craters for these two events exhibit remarkably similar topologies. More to the point, these two craters appear to be on the verge of forming a reentrant shape. That is, the shapes are not reentrant, but it seems clear that a slightly larger impact energy would result in a reentrant cavity. Hence, it is possible that the velocities at which the two systems explored in this paper begin to show a non-zero deposition efficiency coincide with the impact velocities at which reentrant cavities begin to form, creating a rivet-like particle/cavity assembly.

5. Conclusions

Based on the results obtained in the present work, the following main conclusions can be drawn:

1. The critical velocity, above which cold-spray deposition takes place is associated with the attainment of a condition for the formation of a particle/substrate interfacial jet composed of both the particle material and the substrate material.
2. Higher particle/substrate contact pressures and better developed interfacial jets, both attainable through larger kinetic energies of the particle, appear to be the major factors controlling the strength of interfacial bonding and the deposition efficiency.
3. An interfacial instability due to differing viscosities and the resulting interfacial roll-ups and vortices may promote interfacial bonding by increasing the interfacial area, giving rise to material mixing at the interface and by providing mechanical interlocking between the two materials.
4. A particle-length scale rivet-like mechanism may also be operative and its onset may be linked with the minimum critical particle velocity.

Acknowledgements

The material presented in this paper is based on work supported by the US Army Grant Number DAAD19-01-1-0661. The authors are indebted to Drs. Walter Roy and Fred Stanton of the ARL for the support and a continuing interest in the present work. The authors also acknowledge the support of the Office of High Performance Computing Facilities at Clemson University.

References

[1] A.P. Alkhimov, A.N. Papyrin, V.F. Dosarev, N.I. Nestorovich M.M. Shuspanov, Gas dynamic spraying method for applying a coating, US Patent 5,302,414 (12 April 1994).

[2] A.O. Tokarev, Structure of aluminum powder coatings prepared by cold gas dynamic spraying, Met. Sci. Heat Treat 35 (1996) 136.

[3] R.C. McCune, A.N. Papyrin, J.N. Hall, W.L. Riggs, P.H. Zajchowski, An exploration of the cold gas-dynamic spray method for several material systems, in: C.C. Berndt, S. Sampath (Eds.), Thermal Spray Science and Technology, ASM International, 1995, pp. 1–5.

[4] C.V. Bishop, G.W. Loar, Practical pollution abatement method for metal finishing, Plat. Surf. Finish. 80 (1993) 37.

[5] D.L. Gilmore, R.C. Dykhuizen, R.A. Neiser, T.J. Roemer, M.F. Smith, Particle velocity and deposition efficiency in the cold spray process, J. Therm. Spray Technol. 8 (1999) 576.

[6] V. Shukla, G.S. Elliot, B.H. Kear, Nanopowder deposition by supersonic rectangular jet impingement, J. Therm. Spray Technol. 9 (2000) 394.

[7] T.H. Van Steenkiste, J.R. Smith, R.E. Teets, J.J. Moleski, D.W. Gorkiewicz, R.P. Tison, D.R. Marantz, K.A. Kowalsky, W.L. Riggs II, P.H. Zajchowski, B. Pilsner, R.C. McCune, K.J. Barnett, Kinetic cold spray coatings, in: Surface and Coatings Technology, Elsevier, Amsterdam, 1999, pp. 62–71.

[8] M.F. Smith, J.E. Brockmann, R.C. Dykhuizen, D.L. Gilmore, R.A. Neiser, T.J. Romer, Solid, freeform and additive fabrication, in: D. Dimos, S.C. Danforth, M. Cima (Eds.), in: Proceedings of the Material Research Society Fall Meeting, Boston, MA, 1998, pp. 65–76.

[9] R.C. Dykhuizen, M.F. Smith, D.L. Gilmore, R.A. Neiser, X. Jiang, S. Sampath, Impact of high velocity cold spray particles, J. Therm. Spray Technol. 8 (1999) 559.

[10] E.S. Hertel, R.L. Bell, M.G. Elrick, A.V. Farnsworth, G.I. Kerley, J.M. McGlaun, S.V. Petney, S.A., Silling, L. Yarrington, Lance CTH: a software family for multi-dimensional shock physics analysis, in: Presentation at 19th International Symposium on Shock Waves, Marseille, France, 26–30 July, 1993.

[11] I. Kerley, Theoretical equations of state for the detonation properties of explosives, in: J.M. Short (Ed.), Proceedings of the Eighth International Symposium on Detonation, Naval Surface Weapons Centre (NSWL MP 86-194), White Oak, MD, 1986, pp. 540–547.

[12] D.J. Steinberg, S.G. Cochran, M.W. Guinan, A constitutive model for metals applicable at high strain rate, J. Appl. Phys. 51 (1980) 1498.

[13] D.J. Steinberg, C.M. Lund, A constitutive model for strain rates from 10^{-4} to 10^{6} s^{-1}, J. Appl. Phys. 65 (1989) 1528.

[14] F.J. Zerilli, R.W. Armstrong, Dislocation-mechanics-based constitutive relations for material dynamics calculations, J. Appl. Phys. 61 (1987) 1816.

[15] R.D. Kreig, D.B. Kreig, Accuracies in numerical solution methods for the elastic perfectly-plastic model, J. Pressure Vessel Technol. ASME 99 (1977) 510.

[16] T.H. Van Steenkiste, J.R. Smith, R.E. Teets, Aluminum coatings via kinetic spray with relatively large powder particles, Surf. Coat. Technol. 154 (2002) 237.

[17] H. El-Sobky, Mechanics of explosive welding, in: T.Z. Blazynski (Ed.), Chapter 6 of Explosive Welding, Forming and Compaction, Applied Science Publishers, London, 1983.

[18] M. Grujicic, G.B. Olson, W.S. Owen, Mobility of the β_1–γ_1 martensitic interface in Cu–Al–Ni. I. Experimental measurements, Metall. Trans. 16 (1985) 1723.

[19] C.S. Yih, Instability due to viscosity stratification, J. Fluid Mech. 27 (1967) 337.